Efficient continuous-wave four-wave mixing in bandgap-engineered AlGaAs waveguides

Jeremiah J. Wathen,[1,2,]* Paveen Apiratikul,[1,3] Christopher J. K. Richardson,[1] Gyorgy A. Porkolab,[1,3]
Gary M. Carter,[1,4] and Thomas E. Murphy[1,3,5]

[1]Laboratory for Physical Sciences, College Park, Maryland 20740, USA

[2]Department of Physics, University of Maryland, College Park, Maryland 20742, USA

[3]Department of Electrical & Computer Engineering, University of Maryland, College Park, Maryland 20742, USA

[4]Department of Electrical & Computer Engineering, University of Maryland Baltimore County, Baltimore, Maryland 21250, USA

[5]Institute for Research in Electronics & Applied Physics, University of Maryland, College Park, Maryland 20742, USA

*Corresponding author: wathenjj@lps.umd.edu

We present a side-by-side comparison of the nonlinear behavior of four passive AlGaAs ridge waveguides where the bandgap energy of the core layers ranges from 1.60 to 1.79 eV. By engineering the bandgap to suppress two-photon absorption, minimizing the linear loss, and minimizing the mode area, we achieve efficient wavelength conversion in the C-band via partially degenerate four-wave mixing with a continuous-wave pump. The observed conversion efficiency [Idler(OUT)/Signal(IN) = −6.8 dB] is among the highest reported in passive semiconductor or glass waveguides. © 2014 Optical Society of America

OCIS codes: (190.4360) Nonlinear optics, devices; (190.4380) Nonlinear optics, four-wave mixing; (190.4400) Nonlinear optics, materials; (230.4320) Nonlinear optical devices; (230.7370) Waveguides; (230.7405) Wavelength conversion devices.

http://dx.doi.org/10.1364/OL.39.003161

Four-wave mixing in optical fiber has long been used to achieve wavelength conversion in the telecom spectrum [1,2]. However, the weak nonlinearity of silica glass requires long spans of fiber to achieve efficient wavelength conversion, which prevents integration of fiber-based wavelength converters into ever-shrinking photonic systems. Chip-based waveguides could enable all-optical wavelength conversion in a compact, integrated platform, greatly simplifying wavelength management in optical networks. $Al_xGa_{1-x}As$ is a promising material for nonlinear waveguides because it has a large third-order susceptibility, and its bandgap can be adjusted by controlling the mole fraction x in the alloy. Both the nonlinear refractive index (n_2) and the two-photon-absorption (2PA) coefficient (α_2) increase as the photon energy approaches the half-bandgap [3–5]. By engineering the bandgap of the waveguide's core, it is possible to suppress 2PA while maintaining a large refractive nonlinearity [6,7].

While it is well known that suppression of nonlinear absorption can be achieved by tailoring the bandgap, the wavelength conversion efficiency in this material system has lagged behind that of more established waveguide platforms—even those that suffer from nonlinear absorption. By engineering the bandgap and reducing the mode area and linear loss, we achieve a continuous-wave (CW) conversion efficiency of -6.4 ± 0.1 dB measured at the output, or -6.8 ± 1.2 dB measured relative to the input signal. (The larger uncertainty for the latter stems from the compounded uncertainties in partitioning the numerous contributions to the insertion loss.) This result is comparable with the highest reported CW conversion efficiency achieved in passive semiconductor or glass waveguides [8–11].

We studied several bandgap-engineered passive AlGaAs ridge waveguides by conducting nonlinear transmission measurements (using a pulsed laser) and four-wave-mixing (FWM) measurements (using two CW lasers). The bandgap of the waveguide-cores ranges from $E_g = 1.60$ eV, where 2PA should occur for $\lambda \leq 1550$ nm, to $E_g = 1.79$ eV, where 2PA becomes significant for $\lambda \leq 1386$ nm. The effective mode areas, where $A_{\text{eff}} \equiv (\iint |E(x,y)|^2 \mathrm{d}x\mathrm{d}y)^2 / \iint |E(x,y)|^4 \mathrm{d}x\mathrm{d}y$, and the group-velocity-dispersion (GVD) parameters were estimated using a finite-difference mode-solver. The calculated GVD parameters range from $\beta_2 = 0.45 \pm 0.05$ ps^2/m for Waveguide IV to $\beta_2 = 1.05 \pm 0.05$ ps^2/m for Waveguide I. The linear loss of each waveguide was measured at 1550 nm using the Fabry–Pérot technique [12]. Figure 1 shows a representative scanning electron micrograph and waveguide cross section. Figure 2 shows the specific properties of each waveguide.

We confirmed the absence of 2PA in Waveguide II by comparing the power-dependent transmission of short pulses through Waveguide I to Waveguide II. Pulses from
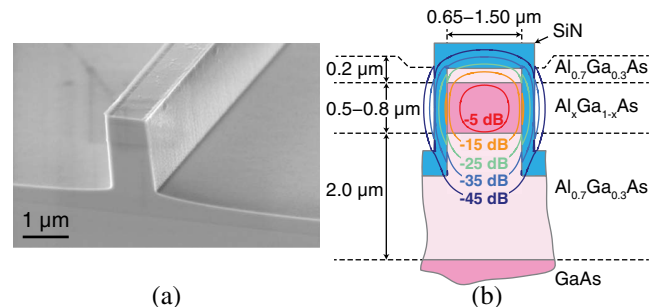

Fig. 1. (a) Micrograph of a typical AlGaAs waveguide (prior to antireflection coating). (b) A representative cross-section, showing typical layer compositions and dimensions. The contours are the calculated TE optical mode for a core of width 1.2 μm and height 0.8 μm, and mole fraction $x = 0.17$.
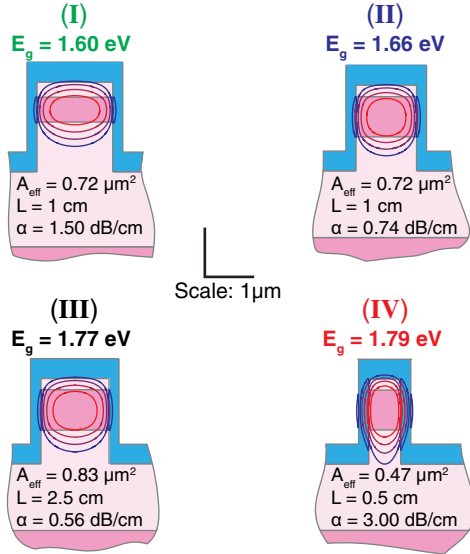
(I)
E_g = 1.60 eV

A_{eff} = 0.72 μm²
L = 1 cm
α = 1.50 dB/cm

(II)
E_g = 1.66 eV

A_{eff} = 0.72 μm²
L = 1 cm
α = 0.74 dB/cm

Scale: 1μm

(III)
E_g = 1.77 eV

A_{eff} = 0.83 μm²
L = 2.5 cm
α = 0.56 dB/cm

(IV)
E_g = 1.79 eV

A_{eff} = 0.47 μm²
L = 0.5 cm
α = 3.00 dB/cm

Fig. 2. Cross-sections and properties of the waveguides, labeled I to IV in order of ascending core-bandgap energy. The contours are the −5 through −20 dB levels of the calculated TE optical mode.

a mode-locked fiber laser with a repetition rate of 10 MHz were launched into the TE eigenstate of each waveguide. The pulse-envelopes were approximately hyperbolic-secant-squared, $P(t) = P_0 \text{sech}^2(t/t_0)$, with $t_0 = 0.63$ ps and a center-wavelength of 1550 nm. Figure 3 shows the inverse transmission ($P_{avg}^{in}/P_{avg}^{out}$) versus the inserted intensity. The dispersion length for these waveguides, $L_D = t_0^2/|\beta_2|$, is much longer than the physical length. We therefore neglect pulse-broadening effects and model the propagation of the pulse-envelope through distance z according to

$$\frac{\partial I(z,t)}{\partial z} = -\alpha I(z,t) - \alpha_2 I^2(z,t) - \alpha_3 I^3(z,t), \quad (1)$$

where $I(z,t)$ is the intensity, α is the linear loss, and α_2 and α_3 represent nonlinear absorption. In this respect,
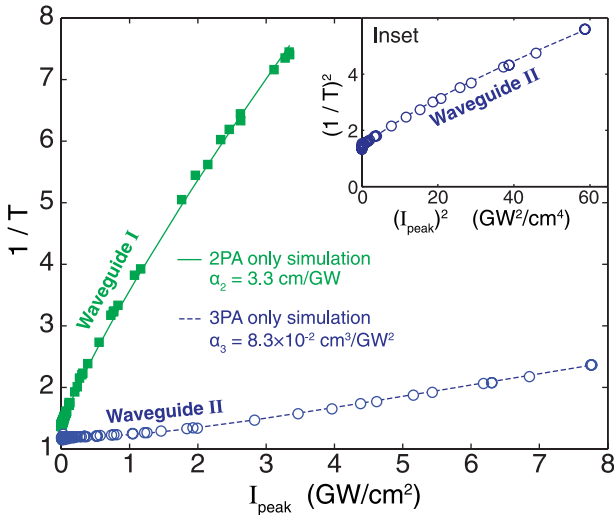

Fig. 3. Measured and simulated inverse transmission versus peak input intensity for Waveguides I and II. Inset: Inverse transmission squared versus the square of peak input intensity for Waveguide II.

the nonlinear absorption coefficients are "effective" coefficients in that they include contributions from multi-photon absorption and free-carrier absorption.

Waveguide I exhibits significant 2PA and shows a nearly linear relation in $1/T$ versus input intensity. The slight curvature of the trend results from modification of the pulse shape due to preferential nonlinear absorption of the pulse-center. For this intensity-regime ($I \ll \alpha_2/\alpha_3$), the three-photon-absorption (3PA) term may be neglected, and Eq. (1) can be integrated to yield $I(L,t) = e^{-\alpha L}I(0,t)/(1 + \alpha_2 I(0,t)L_{eff})$, where L is the waveguide's physical length and $L_{eff} = (1 - e^{-\alpha L})/\alpha$ is the effective nonlinear length. For a sech² pulse, where $I(0,t) = I_0 \text{sech}^2(t/t_0)$, we have [13]

$$\frac{1}{T} = \frac{e^{\alpha L}(1 + \alpha_2 L_{eff} I_0)^{\frac{1}{2}}(\alpha_2 L_{eff} I_0)^{\frac{1}{2}}}{\ln[(1 + \alpha_2 L_{eff} I_0)^{\frac{1}{2}} + (\alpha_2 L_{eff} I_0)^{\frac{1}{2}}]}. \quad (2)$$

By adjusting α_2 as a free parameter and matching the simulation to the data, we estimate $\alpha_2 = 3.3$ cm/GW for Waveguide I.

The core-bandgap for Waveguide II is 1.66 eV, and 2PA should be absent for wavelengths significantly longer than 1494 nm. Indeed, the small slope and upward curvature of the $1/T$ data suggest 2PA is negligible. Additionally, when we instead plot $(1/T)^2$ versus I_{peak}^2 (see the inset in Fig. 3) we see a nearly linear trend, which is to be expected in a system dominated by 3PA. Neglecting the 2PA term, Eq. (1) takes the solution $I(L,t) = e^{-\alpha L}I(0,t)/[1 + (\alpha_3/\alpha)I^2(0,t)(1 - e^{-2\alpha L})]^{\frac{1}{2}}$, and the transmittance for a sech² pulse becomes

$$T = \int_{-\infty}^{\infty} \frac{\frac{1}{2t_0} e^{-\alpha L}\text{sech}^2\left(\frac{t}{t_0}\right)\text{d}t}{\left[1 + \frac{\alpha_3}{\alpha}I_0^2 \text{sech}^4\left(\frac{t}{t_0}\right)(1 - e^{-2\alpha L})\right]^{\frac{1}{2}}}. \quad (3)$$

By numerically integrating Eq. (3) and adjusting α_3 as a free parameter to match the data, we estimate $\alpha_3 = 8.3 \times 10^{-2}$ cm³/GW², in good agreement with published values [14]. Again, the model presented in Eq. (1) does not explicitly isolate the impact of free-carrier absorption, so the nonlinear coefficient determined here represents an overestimate of the true 3PA coefficient.

Figure 4 shows the output spectra for different input powers, obtained using the same pulsed laser used during the nonlinear transmission experiments. The spectra for Waveguide I become asymmetric and exhibit a blue-shift, characteristic of the spectral shift caused by free carriers. The spectra for Waveguide II display a larger nonlinear phase shift for a given power because it possesses smaller linear and nonlinear losses. The split-step Fourier transform method was used to simulate the spectra for Waveguide II. The simulations include the effects of Kerr refraction and 3PA, with $n_2 = 1.45 \times 10^{-4}$ cm²/GW and $\alpha_3 = 8.3 \times 10^{-2}$ cm³/GW².

To measure the CW FWM efficiency, two CW lasers were separately amplified to produce the pump and signal, respectively. The wavelength range over which efficient FWM can be achieved is constrained by the dispersion, device length, and the pump power [15].
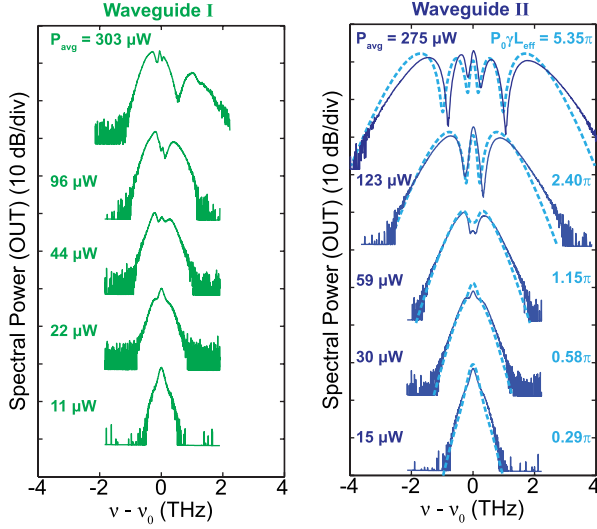
Fig. 4. Measured output spectra (solid lines) for Waveguides I and II, offset for clarity. Labels on the left of each column indicate the average power launched into the waveguide. The dashed cyan lines are simulations of the spectra for Waveguide II, and cyan labels on the right indicate the simulated peak phase shift.

For a pump power of 100 mW, we estimated the FWM bandwidth of each waveguide by numerically solving Eqs. (4), below. The calculated bandwidths range from $\Delta\lambda_{\max} = 13$ nm for the longest waveguide (III) to $\Delta\lambda_{\max} = 44$ nm for the shortest waveguide (IV). Here, $\Delta\lambda_{\max}$ denotes the wavelength difference between the pump and signal at which the conversion efficiency falls by −3 dB. For the measurements presented in the following discussion, $\Delta\lambda$ was fixed at less than 1 nm to ensure nearly perfect phase matching in the low-pump-power limit. The nonlinear contribution to the phase-mismatch is negligible at low pump powers, but is moderately important at the highest pump powers used in Waveguide III. A 50/50 PM coupler combined the co-polarized pump and signal waves, which were launched into the waveguide through a PM lensed fiber, exciting only the TE eigenstate. A 95/5 tap coupler immediately prior to the waveguide was used to monitor the input power and spectrum. At the waveguide's output, a second lensed fiber and tap coupler collected the idler, signal, and pump to measure the output power and spectrum.

The interaction among the pump, signal, and idler is described by the following propagation equations [2,16]

$$\frac{dP_p}{dz} = -\alpha P_p - \frac{\alpha_2}{A_{\text{eff}}}(P_p + 2P_s + 2P_i)P_p$$
$$-4\frac{\omega n_2}{cA_{\text{eff}}}P_p\sqrt{P_sP_i}\sin\theta - 2\frac{\alpha_2}{A_{\text{eff}}}P_p\sqrt{P_sP_i}\cos\theta, \quad (4a)$$

$$\frac{dP_s}{dz} = -\alpha P_s - \frac{\alpha_2}{A_{\text{eff}}}(2P_p + P_s + 2P_i)P_s$$
$$+2\frac{\omega n_2}{cA_{\text{eff}}}P_p\sqrt{P_sP_i}\sin\theta - \frac{\alpha_2}{A_{\text{eff}}}P_p\sqrt{P_sP_i}\cos\theta, \quad (4b)$$

$$\frac{dP_i}{dz} = -\alpha P_i - \frac{\alpha_2}{A_{\text{eff}}}(2P_p + 2P_s + P_i)P_i$$
$$+2\frac{\omega n_2}{cA_{\text{eff}}}P_p\sqrt{P_sP_i}\sin\theta - \frac{\alpha_2}{A_{\text{eff}}}P_p\sqrt{P_sP_i}\cos\theta, \quad (4c)$$

and

$$\frac{d\theta}{dz} = (k_s + k_i - 2k_p) + \frac{\omega n_2}{cA_{\text{eff}}}(2P_p - P_s - P_i)$$
$$+ \frac{\omega n_2}{cA_{\text{eff}}}\left(P_p\sqrt{\frac{P_s}{P_i}} + P_p\sqrt{\frac{P_i}{P_s}} - 4\sqrt{P_sP_i}\right)\cos\theta$$
$$+ \frac{\alpha_2}{A_{\text{eff}}}\left(P_p\sqrt{\frac{P_s}{P_i}} + P_p\sqrt{\frac{P_i}{P_s}} - 4\sqrt{P_sP_i}\right)\sin\theta, \quad (4d)$$

where P_m and k_m, $m = \{p, s, i\}$ represent the powers and propagation constants of the pump, signal, and idler waves; ω is the optical center frequency; and $\theta(z)$ represents the local phase mismatch. In the low-conversion-efficiency regime ($P_p \gg P_s \gg P_i$), assuming zero phase mismatch, Eqs. (4) yield an approximate solution for the conversion efficiency

$$\frac{P_i(L)}{P_s(0)} = e^{-\alpha L}\left(|\gamma|P_{p0}L_{\text{eff}}\right)^2, \quad (5)$$

where $\gamma = ((\omega/c)n_2 + i(\alpha_2/2)/A_{\text{eff}}$ is the complex nonlinear parameter and P_{p0} is the inserted pump power.

As shown in Fig. 5, to compare only the nonlinear properties of the waveguides, we normalize-out the linear properties by plotting the conversion efficiency versus the quantity $(L_{\text{eff}}/A_{\text{eff}})e^{-(\alpha L/2)}P_{p0}$. Initially, Waveguide I generates the largest conversion efficiency because it has the largest $|(\omega/c)n_2 + i(\alpha_2/2)|$. However, nonlinear absorption limits the achievable conversion efficiency. In contrast, nonlinear absorption is negligible for Waveguides II through IV and the conversion efficiency scales quadratically up to the damage threshold of the waveguide. The highest conversion efficiency was obtained in Waveguide III. (The output spectrum is shown in the inset.) This waveguide possesses the unique combination of small 2PA, small linear loss, and a large physical length, which allowed the insertion of significantly more pump power (up to 630 mW) without damage to the device.

The straight lines in Fig. 5 show the low-efficiency scaling relationships according to Eq. (5). The positions of these lines depend only on $|(\omega/c)n_2 + i(\alpha_2/2)|$. Because both n_2 and α_2 decrease as the bandgap increases, these lines are ordered in increasing bandgap from top-left to bottom-right. The scaling relationship for Waveguide I was calculated using $\alpha_2 = 3.3$ cm/GW and $n_2 = 2.3 \times 10^{-4}$ cm^2/GW. For Waveguides II, III, and IV, the scaling relationships use $\alpha_2 = 0$, and $n_2 = 1.45 \times 10^{-4}$, 0.90×10^{-4}, and 0.85×10^{-4} cm^2/GW, respectively. The bandgap-dependence of these coefficients is in good
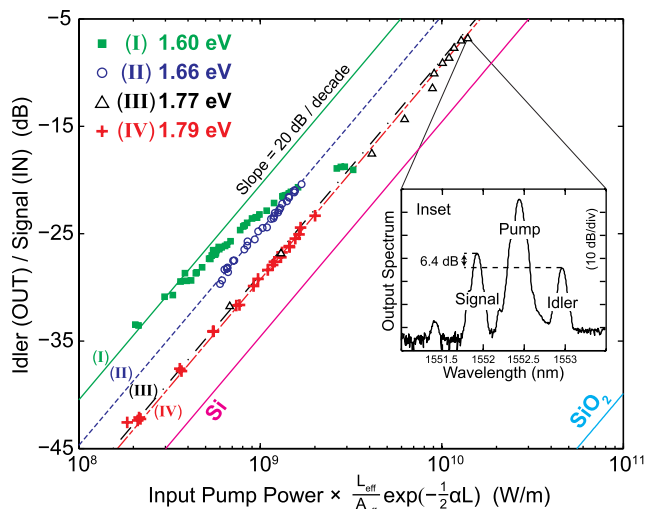
Fig. 5. CW FWM efficiency versus $P_{p0} \times (L_{eff}/A_{eff})e^{-(\alpha L/2)}$. Symbols represent the measured efficiencies and the lines were calculated using Eq. (5). Inset: The output spectrum observed for the highest conversion efficiency.

agreement with published values [5,7]. Included for comparison are the relationships expected for silicon ($\alpha_2 = 0.79$ cm/GW and $n_2 = 0.45 \times 10^{-4}$ cm^2/GW [17]) and silica glass ($\alpha_2 = 0$ and $n_2 = 0.002 \times 10^{-4}$ cm^2/GW [18]).

In conclusion, by engineering the bandgap of AlGaAs to suppress 2PA and simultaneously reducing linear propagation losses and mode area, we achieve efficient wavelength conversion via continuous-wave four-wave mixing. The obtained conversion efficiency rivals the highest CW efficiency previously reported for passive semiconductor or glass waveguides.

References

1. K. Inoue and H. Toba, IEEE Photon. Technol. Lett. **4**, 69 (1992).
2. J. Handsryd, P. A. Andrekson, M. Westlund, J. Li, and P.-O. Hedekvist, IEEE J. Sel. Top. Quantum Electron. **8**, 506 (2002).
3. M. Sheik-Bahae, D. C. Hutchings, D. J. Hagan, and E. W. V. Stryland, IEEE J. Quantum Electron. **27**, 1296 (1991).
4. A. Villeneuve, C. C. Yang, G. I. Stegeman, C.-H. Lin, and H.-H. Lin, Appl. Phys. Lett. **62**, 2465 (1993).
5. J. S. Aitchison, D. C. Hutchings, J. U. Kang, G. I. Stegeman, and A. Villeneuve, IEEE J. Quantum Electron. **33**, 341 (1997).
6. K. Dolgaleva, W. C. Ng, L. Qian, J. S. Aitchison, M. C. Camasta, and M. Sorel, Opt. Lett. **35**, 4093 (2010).
7. K. Dolgaleva, W. C. Ng, L. Qian, and J. S. Aitchison, Opt. Express **19**, 12440 (2011).
8. W. Mathlouthi, H. Rong, and M. Paniccia, Opt. Express **16**, 16735 (2008).
9. K. Y. Wang and A. C. Foster, Opt. Lett. **37**, 1331 (2012).
10. M. D. Pelusi, F. Luan, S. Madden, D.-Y. Choi, D. A. Bulla, B. Luther-Davies, and B. J. Eggleton, IEEE Photon. Technol. Lett. **22**, 3 (2010).
11. J. S. Levy, A. Gondarenko, M. A. Foster, A. C. Turner-Foster, A. L. Gaeta, and M. Lipson, Nat. Photonics **4**, 37 (2010).
12. E. Kapon and R. Bhat, Appl. Phys. Lett. **50**, 1628 (1987).
13. J. Matres, C. Lacava, G. C. Ballesteros, P. Minzioni, I. Cristiani, J. M. Fédéli, J. Martí, and C. J. Oton, Opt. Express **20**, 23838 (2012).
14. J. U. Kang, A. Villeneuve, M. Sheik-Bahae, G. I. Stegeman, K. Al-hemyari, J. S. Aitchison, and C. N. Ironside, Appl. Phys. Lett. **65**, 147 (1994).
15. N. Shibata, R. P. Braun, and R. G. Waarts, IEEE J. Quantum Electron. **QE-23**, 1205 (1987).
16. K. Inoue and T. Mukai, Opt. Lett. **26**, 10 (2001).
17. M. Dinu, F. Quochi, and H. Garcia, Appl. Phys. Lett. **82**, 2954 (2003).
18. G. P. Agrawal, *Nonlinear Fiber Optics*, 5th ed. (Academic, 2012).